Aerosol nanoparticles in the $Fe_{1-x}Cr_x$ system: Room-temperature stabilization of the σ phase and $\sigma \rightarrow \alpha$-phase transformation

M. Gich
Institut de Ciència de Materials de Barcelona-Consell Superior d'Investigacions Científiques (ICMAB-CSIC), Esfera UAB, 08193 Bellaterra, Catalunya, Spain

E. A. Shafranovsky
Semenov Institute of Chemical Physics, Russian Academy of Sciences, Kosyguin Str. 4, 119991, GSP-1, Moscow, Russia

A. Roig[a)]
Institut de Ciència de Materials de Barcelona-Consell Superior d'Investigacions Científiques (ICMAB-CSIC), Esfera UAB, 08193 Bellaterra, Catalunya, Spain

A. Ślawska-Waniewska and K. Racka
Institute of Physics, Polish Academy of Sciences, Aleja Lotników 32/46, 02-668 Warsaw, Poland

Ll. Casas
Institut de Ciència de Materials de Barcelona-Consell Superior d'Investigacions Científiques (ICMAB-CSIC), Esfera UAB, 08193 Bellaterra, Catalunya, Spain and Geomagnetism Laboratory, Oliver Lodge Building, Oxford Street, University of Liverpool, Liverpool L69 7ZE, United Kingdom

Yu. I. Petrov
Semenov Institute of Chemical Physics, Russian Academy of Sciences, Kosyguin Str. 4, 119991, GSP-1, Moscow, Russia

E. Molins
Institut de Ciència de Materials de Barcelona-Consell Superior d'Investigacions Científiques (ICMAB-CSIC), Esfera UAB, 08193 Bellaterra, Catalunya, Spain

M. F. Thomas
Department of Physics, University of Liverpool, Liverpool L69 7ZE, United Kingdom

(Received 4 March 2005; accepted 10 May 2005; published online 19 July 2005)

The production and structural characterization of gas-evaporated nanoparticles in the $Fe_{1-x}Cr_x$ system, with $0<x<0.83$ are reported. The results show that for $x\sim0.5$ the metastable σ-FeCr can be stabilized and it constitutes up 60 wt % of the material. The sample with the highest σ-FeCr content is further analyzed to study the structural and the magnetic properties of this phase and its thermal stability. The σ-FeCr phase is weakly magnetic with an average magnetic moment of $0.1\mu_B$ per Fe atom and a Curie temperature below $\sim$60 K. It is stable up to 550 K where it starts to transform to bcc-FeCr. Annealing at 700 K yields Cr_2O_3 due to Cr surface segregation and affects the magnetic behavior of the system, which is dominated by interparticle interactions. © *2005 American Institute of Physics*. [DOI: 10.1063/1.1946907]

I. INTRODUCTION

The development of techniques such as gas phase synthesis and rapid solidification has enabled the production of alloys with more uniform and refined microstructures leading to an improvement of its mechanical, magnetic, or catalytic properties.[1] Moreover, the microstructural reduction down to the nanometric regime has also opened the door to many investigations and applications since, resulting from the fast kinetics involved in these processes, a number of high-temperature phases can be stabilized at room temperature. However, the appearance of some of these metastable phases is sometimes undesirable and the control of phase separation is the subject of many investigations in metallurgy. The tetragonal σ-FeCr phase, responsible for the so-called "475 °C embrittlement" in ferritic stainless steels, is one of these metastable phases to be avoided.

Besides displaying good mechanical, anticorrosive,[2] and wear resistance[3] properties, Fe–Cr alloys are also of technological interest as catalysts of the water gas shift reaction that eliminates the CO produced during the fuel cells operation.[4] It has been proposed as a cheaper substitute of $LaCrO_3$ as the interconnect material in solid oxide fuel cells[5] and, as thin films, it is tested for enhancing the magnetoresistance and the thermal stability of synthetic spin valves.[6]

According to the equilibrium phase diagram for the Fe–Cr system[7] (see Fig. 1), a tetragonal σ phase exists as a single phase within a narrow range of Cr concentrations (44.5–50 at. %) at temperatures from 450 to 830 °C. Above 830 °C, Fe–Cr alloy forms a single body-centered-cubic phase (α), whereas at $T<450$ °C, the σ phase disappears

[a)]Author to whom correspondence should be addressed; FAX: +34-935805729; electronic mail: roig@icmab.es

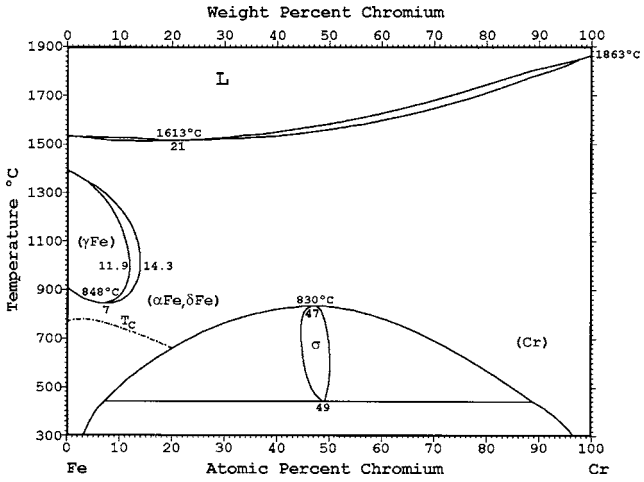

FIG. 1. Fe–Cr binary phase diagram adapted from Massalski (see Ref. 7).

and the alloy decomposes to Fe-rich ferromagnetic (α_1) and Cr-rich paramagnetic (α_2) bcc phases. Nevertheless, this scenario is significantly altered for nanostructured Fe–Cr alloys where a number of nonequilibrium Fe–Cr phases have been reported for fine particles, thin films, as well as in samples prepared by pulsed laser deposition and subsequent prolonged annealing.[8]

The aim of the present study is to show the broad range of compositions where the metastable σ-FeCr phase has been stabilized as nanoparticles and to report on the magnetic properties and thermal stability of the σ phase. For this purpose, Fe–Cr nanoparticles have been produced by gas evaporation technique in the compositional range from 0 to 83.0 at. % Cr. The material was characterized by means of x-ray diffraction (XRD), transmission electron microscopy (TEM), Mössbauer spectroscopy (MS), differential scanning calorimetry (DSC), differential thermal analysis (DTA), and vibrating-sample magnetometry (VSM). It is shown that σ-FeCr is the majority phase for 47.7 at. % Cr. Subsequent thermal treatments yield changes in the particle composition and segregation of Cr, having a pronounced effect on its magnetic properties.

II. EXPERIMENTAL DETAILS

Fe–Cr alloys, containing from 0 to 83.0 at. % of Cr, were produced by direct alloying of components with 99.9% purity, using a 10 kW rf generator at a working frequency of 440 kHz and a specially designed inductor. The latter provided heating to melt a specimen of about 1.5 g and made possible the levitation of the melted drop in an Ar atmosphere. A homogeneous mixture of alloy components was obtained by eddy currents. After exposing the drop at about 2300–2800 K for a few minutes, the generator was turned off and the drop fell off down on a massive copper vessel that assured the quenching of the alloy. An advantage of the inductive alloying method is the absence of any crucible avoiding material contamination. The alloy composition was monitored by weighing the specimen before and after alloying and by x-ray diffraction analysis. Aerosol particles were produced by "gas evaporation" of the initial alloys (predegassed in vacuum) from a tungsten spiral-basket-shaped filament heated by ac power in an Ar atmosphere at 3-Torr pressure. The details of the technique were discussed elsewhere.[9] The aerosol particles were deposited on the walls of a stainless-steel cylinder of 10 cm in diameter that essentially diminished the probability of self-ignition of the nanoparticles, due to high heat removal of the metallic support, upon scraping-off and subsequent exposure of the particles to air. Then, the deposits were kept at a residual air pressure of several Torr for 12 h. This resulted in passivation of the particles with a thin oxide shell making possible further handling of the powder in the ambient atmosphere. The evaporation process was viewed through an inclined mirror placed on a glass plate, which covered the top of the cylinder.

Energy dispersive x-ray analyses (EDX) were performed with a JEOL JSM-6300 scanning microscope equipped with an Oxford Instruments LINK ISIS-200 EDX. The spectroscopic analyses confirmed that no deviations from the master alloy composition occurred during the nanoparticle production by gas evaporation.

Structural characterization was performed by analyzing XRD patterns recorded in a θ-2θ Bragg–Brentano geometry with a Siemens D5000 powder diffractometer with Cu $K\alpha$ incident radiation ($\lambda = 1.5406$ Å) and a graphite monochromator. The XRD data were analyzed by Rietveld refinements using the MAUD program[10] to obtain structural information of the Fe–Cr nanoparticles, i.e., phase contents, crystallite sizes, and cell parameters. The tetragonal σ-FeCr (space-group $P4_2/mnm$) with the Fe and Cr occupancies reported by Yakel,[11] the bcc-Fe (space-group $Im3m$), and, for some samples, the Fe_3O_4 (space-group $Fd3m$) and Cr_2O_3 (space-group R-$3C$) structures have been adopted. XRD analyses were also performed in a Debye–Scherrer camera when the amount of sample was not enough to perform an experiment in the θ-2θ powder diffractometer. In such case a filterless Cr characteristic radiation (tube voltage 33 kV, current 16 mA) was used to take x-ray photographs of samples on a Kodak X-Omat film (exposure 10–15 min) arranged asymmetrically in a conventional 57.3-mm Debye–Scherrer camera.

TEM observations were carried out using a Hitachi H800MT microscope operating at 200 kV. For high-resolution TEM (HRTEM) studies, a Phillips CM30 microscope operating at 300 kV was used. Before the TEM observations, the samples were ultrasonically dispersed in ethanol, one drop of the solution was deposited onto TEM Cu grids coated with a conductive polymer and the ethanol was let to evaporate.

Mössbauer spectra were acquired at 300, 80, and 4.2 K using a conventional transmission Mössbauer spectrometer with a ^{57}Co/Rh source. Velocity calibration was done using a 25-μm foil of metallic iron, and the Mössbauer parameters are given relative to this standard at room temperature. In-field Mössbauer spectra were taken at 4.2 K in applied fields of 4 and 9 T using a superconducting magnet with the gamma ray beam directed between the coils, normal to the direction of the applied field. Program packages NORMOS (Ref. 12) and FFITA were used to fit the spectra.

For the thermal analysis, a Perkin–Elmer DSC-7 apparatus was used from room temperature to 650 K (20 K/min heating rate) under an Ar atmosphere.

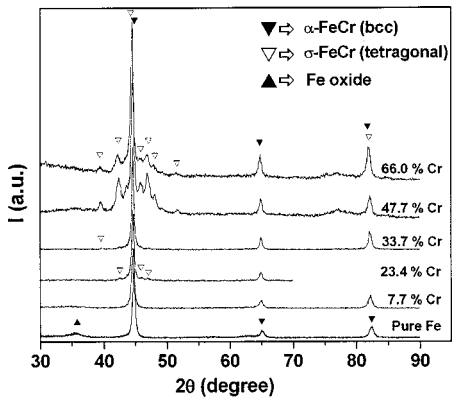

FIG. 2. XRD patterns of FeCr nanoparticles in the 0–66 at. % Cr range.

Magnetic studies were performed with a vibrating-sample magnetometer (Oxford Instruments Ltd.) over the temperature range of 4.2–900 K in an applied field up to 1.1 T.

III. RESULTS AND DISCUSSION

A. Structural characterization of the samples

The XRD patterns of samples with Cr content in the range of 0–66 at. % are presented in Fig. 2. The spectra consist of broad peaks that reveal the nanocrystalline nature of the particles produced by gas evaporation. As shown in the figure, the cubic α-FeCr (also metastable at room temperature) is the major phase in samples with a low Cr content, whereas for samples richer in Cr this phase coexists with the tetragonal σ-FeCr. In the past, metastable σ-FeCr phase has been detected at room temperature in sputtered thin films[13–15] and in alloys with additions of a third element (e.g., Ti, Al, and Sn) [16–19] or after subjecting α-FeCr to long thermal treatments.[20–22] However, as previously shown by Petrov and co-workers,[23,24] nanoparticles of high-temperature phases of metals and alloys can be stabilized at room temperature by gas evaporation. Figure 3 presents the dependencies of the σ-phase content and the α-FeCr lattice parameter on the sample composition, as obtained from Rietveld refinements of the diffraction data. The largest σ-FeCr volume fractions (0.59–0.44) were found in the 47.7–60.4 at. % Cr range. However, the sigma phase, with volume fractions below 10%, was also detected in samples with 83.0, 66.0, 33.7, and 23.4 at. % Cr. Note that, contrary to what one may expect, the latter sample contains more σ-FeCr than the sample with 33.7 at. % Cr, which is closer to the compositional range where the σ phase becomes dominating (see Figs. 2 and 3). This behavior indicates that for samples with lower Cr content the precipitation of small amounts of σ-FeCr (i.e., below 10 vol %) is due to compositional inhomogeneities during the evaporation process. Such chemical fluctuations may result in the formation of some Cr-richer particles for which the formation of the σ phase is indeed prevailing. Thus, it can be concluded that the metastable σ-FeCr is kinetically favored at least in the 47.7–60.4 at. % Cr range. Similar results have been found for sputtered Fe–Cr thin films[13–15] reporting the formation of σ-FeCr as a major phase in the 38–44, 50–58, and 45–55 at. % Cr ranges, with no trace of this phase for Cr contents below 32 and above 68 at. %. In contrast, no σ-FeCr has been found in films deposited by laser ablation in high vacuum ($\sim 10^{-8}$ Torr), in which effective cooling rates as high as 10^{11} K/s are achieved.[8] Figure 3 also shows that the α-FeCr lattice parameter increases with the Cr content as expected from Vegard's law, which has been plotted for comparison (dotted line). This indicates that for all the studied compositions, a single bcc phase (the stable phase at $T > 1100$ K) has been stabilized to the detriment of the room-temperature equilibrium Fe- and Cr-rich bcc phases. Confirmation of this hypothesis is the fact that the spectra refinements were less satisfactory when two bcc phases with the Fe and Cr lattice parameters were considered. From Fig. 3 it is clear that the lattice parameter deviates from Vegard's law for most compositions. In fact, we are dealing with at least a three-phase system. On the other hand, the presence of an Fe oxide layer, probably of reduced crystallinity, has been detected by Mössbauer spectroscopy. The presence of this oxide layer causes an increase of the α-FeCr lattice parameter, since Fe ions of the oxide shell deplete iron from the bcc-FeCr crystals. For Cr-rich compositions, a Cr_2O_3 passivation layer is expected in the bcc-FeCr, yielding Fe-enriched cores. Thus, the Fe-enriched (Cr-enriched) cores in the Cr-rich (Fe-rich) compositions explain why bcc lattice parameters at high (low) Cr contents are lower (higher) than expected from Vegard's law.

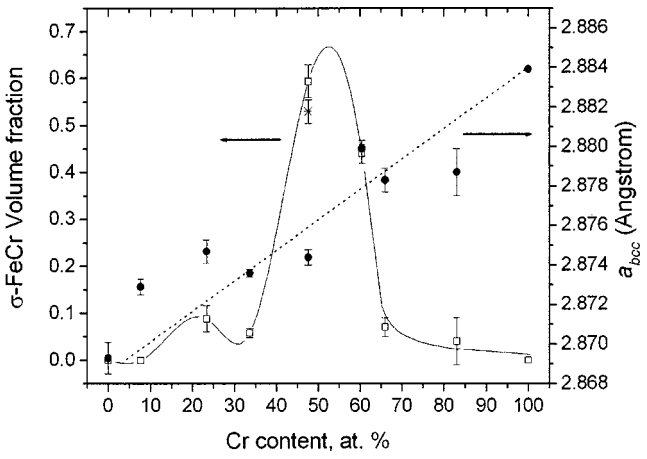

FIG. 3. Nanoparticle phase composition obtained from XRD (□) and Mössbauer spectroscopy (∗) and α-FeCr lattice parameter (●) as a function of the total Cr atomic % content. The continuous line is a guide to the eye. Vegard's law is plotted as a dotted line.

In order to study the thermal stability and the magnetic properties of the σ-FeCr, the sample with the highest volume fraction of this phase (i.e., that containing 47.7 at. % Cr, hereafter referred as FeCr47.7) was selected to make further analyses. A bright-field TEM image of sample FeCr47.7 is presented in Fig. 4. The particles are roughly spherical in shape and form agglomerates. A histogram of the particle size distribution for this sample (see inset) was obtained from several TEM images and fitted to a log-normal distribution function with a maximum at 12.1 nm. The distribution gives an average diameter of 13.7 nm that is increased to 16.7 nm when a volume-weighted distribution is considered. For this sample, the Rietveld refinement analysis re-

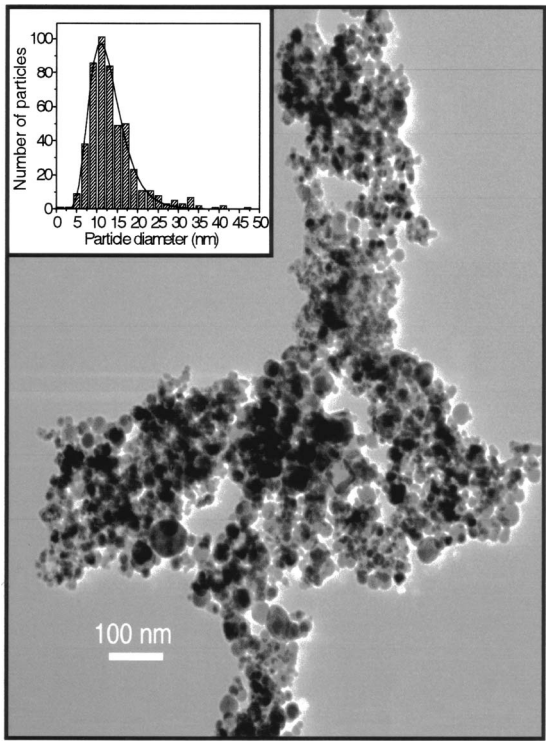

FIG. 4. Bright-field TEM image of Fe–Cr nanoparticles corresponding to FeCr47.7 sample and the particle size histogram. Distribution was fit to a log-normal function.

sults in (i) 35 wt % of α-FeCr bcc with a mean crystallite size $\langle D\rangle_{\alpha\text{-FeCr}} \sim 13$ nm, (ii) 60 wt % of σ-FeCr phase ($\langle D\rangle_{\sigma\text{-FeCr}} \sim 10$ nm), and (iii) 5 wt % Fe_3O_4 with $\langle D\rangle_{Fe_3O_4} < 2$ nm.

B. Thermal stability of σ-FeCr

The stability of the metastable σ phase and its temperature transformation to more stable phases has been studied by DSC and magnetometry. The DSC curve of sample FeCr47.7, presented in Fig. 5, shows an exothermal process starting at about 550 K and lasting until the end of the run at 670 K indicating the transformation of the metastable phase. Indeed, the sample used in the DSC experiment was subsequently analyzed by XRD in a Debye–Scherrer camera and a very strong attenuation of σ-FeCr lines was observed to-

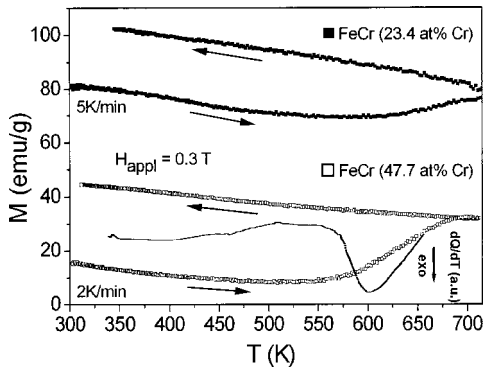

FIG. 5. Magnetization vs temperature for Fe–Cr samples [23.8 (■) and 47.7 (□) at. % Cr]. Heat-flow curve, dQ/dT of Fe–Cr 47.7 at. % Cr in arbitrary units (at a 20-K/min heating rate), is also included.

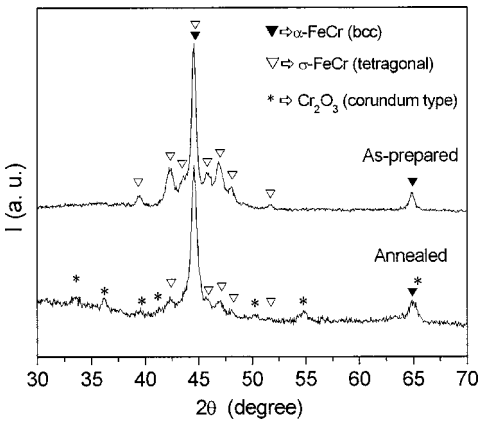

FIG. 6. XRD patterns of FeCr 47.7 at. % Cr as-prepared and annealed at 700 K for 1.5 h.

gether with a significant intensification of the lines corresponding to the bcc phase lines (pattern not shown). These results are supported by the measurements of the temperature dependences of the magnetization, $M(T)$, performed in an applied field of 0.3 T in a heating–cooling cycle in the temperature range of 300–710 K at 2 K/min (see Fig. 5). In a first stage of the heating process, the magnetization presents the behavior of a typical weak ferromagnet, i.e., $M(T)$ monotonically decreases until a minimum is reached at about 530 K. However, a transition to paramagnetism is not seen since it occurs at higher temperature than that of the magnetization increase. Then, the magnetization begins to rise, acquiring a constant rate of increase until about 680 K. The increase of magnetization has the same onset temperature as that of the phase transition revealed by calorimetry, corroborating that it is a $\sigma \rightarrow \alpha$-phase transition, the increase of the volume fraction of the α-FeCr accounting for the raise in magnetization at higher temperatures. In Fig. 5, the $M(T)$ curve for the sample with 23.4 at. % Cr is also plotted. It shows the same behavior as for FeCr47.7, although starting from a higher magnetization value, in accordance with both the larger percentage of α-FeCr phase initially present in that sample and the richer-Fe concentration of this phase. In that case, the relative increase in magnetization is less pronounced than for FeCr47.7, as the amount of the σ phase to be transformed to the bcc one it is smaller.

In order to gain further insight into the $\sigma \rightarrow \alpha$ transition, the as-prepared FeCr47.7 powder was sealed in an evacuated quartz tube and annealed for 1.5 h at 700 K. The XRD patterns corresponding to the as-prepared and annealed samples are presented in Fig. 6. They show that the thermal treatment at 700 K brings about a decrease of the σ-FeCr reflections and the appearance of an additional phase that has been indexed as the corundum-type Cr_2O_3. The Rietveld refinements of the diffraction patterns reveal a decrease, upon annealing at 700 K, in the cell parameter [from 2.8744(4) to 2.8735(4) Å] and the crystallite size (from 13 to 8 nm) of the α-FeCr. This suggests that the thermal treatment has yielded Fe-enriched bcc particles that might result from a process of Cr segregation to the surface of the particles where the Cr oxide would be formed, resulting in a more defined core-shell structure. Actually, the tendency of

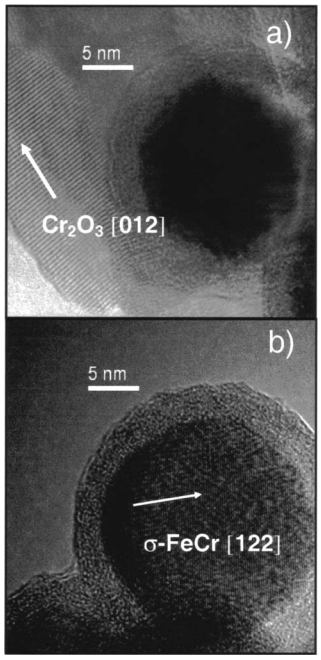

FIG. 7. High-resolution TEM images of the FeCr47.7 sample annealed at 700 K.

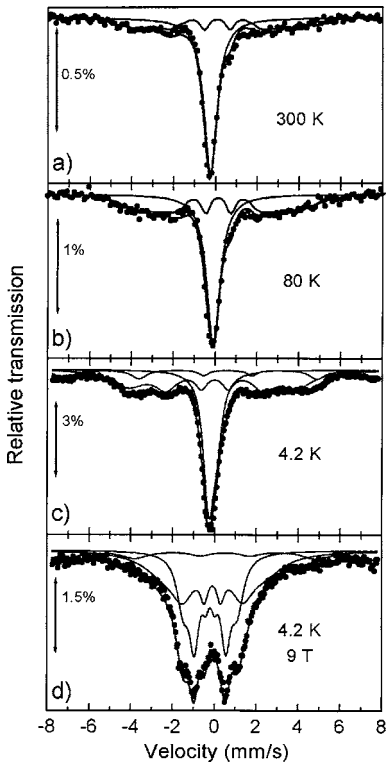

FIG. 8. Mössbauer spectra of as-prepared sample FeCr47.7 at (a) 300, (b) 80, (c) 4.2, and (d) 4.2 K with H_{app}=9 T (applied field perpendicular to γ rays).

Cr surface segregation on heating FeCr alloys has been observed to take place both in air and high vacuum.[25,26] HRTEM images of the annealed sample [see Figs. 7(a) and 7(b)] reveal a core-shell structure of the material. From the Fourier transform of high-resolution images, the phase surrounding the particles could be indexed to Cr_2O_3 in zones where the oxide layer was specially large [see Fig. 7(a)] although this has not been possible in the case of thinner shells [see Fig. 7(b)], where the nature of the oxide cannot unambiguously ascribed to Cr_2O_3. However, the Cr surface-segregation tendency and the Fe enrichment of the core revealed by Mössbauer spectroscopy (Sec. III C) suggest Cr_2O_3 as the main component of the shells. TEM images at low magnification of the annealed material (not shown) revealed a slightly broader particle size distribution deviating from the log-normal function found in the as-prepared sample. Indeed, from the x-ray diffraction pattern of the annealed sample it is found that $\langle D\rangle_{\sigma\text{-FeCr}} \sim 26$ nm, which has been also confirmed by HRTEM [see Fig. 7(b)].

Note that the thermal decomposition of the σ-FeCr is a rather complex process and sensitive to the annealing conditions. Indeed, on the one hand, the XRD of the sample heated up to 670 K in the DSC revealed no traces of Cr_2O_3 and the intensification of bcc phase reflections accompanied by an attenuation of σ-FeCr lines (note that DSC heating cycle lasted for about 20 min). On the other hand, the structural characterization of the sample annealed 1.5 h at 700 K also shows a diminution of the σ phase (from 60 to 30 wt %) and, in addition to this, the appearance Cr_2O_3 and no significant increase in the volume fraction of the bcc phase. These structural changes for the thermally treated sample consequently induce important differences in the magnetic response of the system.

C. Magnetic properties of σ-FeCr

Mössbauer spectra of sample FeCr47.7 recorded at 300, 80, and 4.2 K are shown in Fig. 8. The spectra recorded without applied magnetic field [Figs. 8(a)–8(c)] do not present qualitative changes and have been fitted with a singlet and a broad distribution of hyperfine fields. In the singlet, the contributions of both σ-FeCr and a small fraction of superparamagnetic particles are included, whereas blocked α-FeCr particles account for the distribution of hyperfine fields. The isomer shift of the σ-FeCr component at room temperature [−0.16(6) mm/s] coincides with that reported by Costa *et al.* for nanocrystals obtained from thermally treated ball-milled samples.[27] Due to the progressive blocking of superparamagnetic particles, the relative area of the hyperfine field distribution increases from 31% to 47% of the total resonant area as the temperature is lowered from 300 to 80 K. A sextet representing ~15% of the total resonant area and having the hyperfine parameters of Fe_3O_4 has to be considered in order to fit the 4.2-K spectrum. This would indicate that the superparamagnetic component observed at 300 and 80 K is mainly due to the presence of very fine magnetite crystallites forming a passivation layer at the surface of the particles (<10 wt % Fe_3O_4), in agreement with the Rietveld refinement. It is noteworthy to mention that the amount of iron oxide in sample FeCr47.7 is about one-third of that found for the pure Fe particles of the same size.[28] Upon cooling, the field distribution gets narrower and its average value increases slightly (from 24 T at 300 K to 25 T at 4.2 K), in contrast, the linewidth of the singlet subspectrum widens significantly between 80 and

TABLE I. Effective fields (B_{eff}), isomer shifts (δ_{Fe}) relative to iron, and hyperfine fields (B_{hyp}) for α-FeCr and σ-FeCr phases at 4.2 K obtained from the fittings of the in-field Mössbauer spectra. The errors are given within parentheses and refer to the last digit.

	α-FeCr			σ-FeCr		
$B_{appl.}$ (T)	δ_{Fe} (mm/s)	B_{eff} (T)	B_{hyp} (T)	δ_{Fe} (mm/s)	B_{eff} (T)	B_{hyp} (T)
0	0.04(2)	——	25.0(4)	−0.09(1)	——	1.0(9)
4		22.0(3)	26.0(3)		3.0(6)	1.8(6)
9		15.3(4)	24.3(4)		8.0(2)	1.4(2)

4.2 K, suggesting a magnetic ordering in the σ-FeCr phase at low temperatures. To clarify this point, Mössbauer spectra were recorded at 4.2 K in 4 T and 9 T applied fields. The spectra show sextet components from the α and σ phases which have been fitted assuming the same isomer shift than for the zero-field spectrum and fixing several parameters (hyperfine field and width of the α-FeCr component and relative areas of the subspectra). The fittings reveal that the relative line intensities of the magnetic sextets tend to the ratio 3:4:1:1:4:3 which is already greatly achieved in a 4 T applied field. With the employed experimental geometry, in which the applied field is normal to the gamma ray beam, these intensity ratios indicate alignment of the moments with the applied field direction and suggest a ferromagnetic ordering for both phases. Taking into account the effective hyperfine fields obtained from the spectra fittings and the degree of alignment at 4- and 9-T applied fields, the average hyperfine fields for α and σ phases are found to be around 25 and 1.4 T, respectively (see Table I). The low hyperfine field of the σ component is almost unnoticed without the application of an external field; only at a high external field its value ($\sim$1.4 T) is well defined in the fitting (note the estimated errors in Table I). According to the proportionality between this hyperfine field and the Fe magnetic moment,[29] the latter can be roughly estimated to be $\sim$0.1 Bohr magnetons (μ_B) per Fe atom, confirming the weak ferromagnetism of the sigma phase resulting from intinerant electrons.[30] Figure 9 presents the 80-K Mössbauer spectrum of the annealed FeCr47.7 sample which, as for the spectra of the as-prepared sample, has been fitted to a paramagnetic singlet and a hyperfine field distribution. The σ-FeCr decomposition during annealing at 700 K is reflected by the reduction of the singlet resonant area, which represents about 20% of the total spectrum area compared to the 56% for the as-prepared sample [Figs. 8(b) and 9]. The hyperfine field values of the annealed sample cover a narrower distribution with a maximum field closer to the value for pure Fe (33 T). This contrasts with the broad field distribution of the as-prepared sample and it is in agreement with the XRD data suggesting a Cr depletion from the α-FeCr yielding a particle core of Fe-enriched bcc phase.

Temperature-dependent magnetic measurements were performed on the as-prepared and on the annealed FeCr47.7 samples. The temperature dependencies of the magnetization measured in a 1 T applied field after cooling the sample in zero field are presented in Fig. 10. In fact, this can be taken as the saturation magnetization, M_s, since hysteresis loops measured at different temperatures revealed that this field was strong enough to saturate the samples. The magnetic signal is dominated by the α-FeCr phase and both samples display the magnetization increase at decreasing temperatures expected for ferromagnetic materials. Although the volume fraction of α-FeCr is the same for the two samples, the magnetization values of the annealed powders at room temperature is about three times that of the as-prepared sample, in part because the former has a higher Fe concentration. The insets are blow-ups of the curves in the low-temperature range and show magnetic effects that can be ascribed to the σ-FeCr and Cr_2O_3 phases. For the as-prepared sample, consisting of $\sim$60 wt % σ-FeCr, a gradual increase of magnetization is observed below 80 K. This is due to the contribution of the weakly ferromagnetic σ phase, which has low Curie temperatures (T_C) and small magnetic moments per Fe atom. Namely, the deviation ($\sim$0.35 emu/g) from the trend followed by $M_s(T)$ for $T>80$ K corresponds to an average magnetic moment $\sim 0.1\mu_B$ per Fe atom of the σ-FeCr phase, which is consistent with the values given in the literature.[30,31]

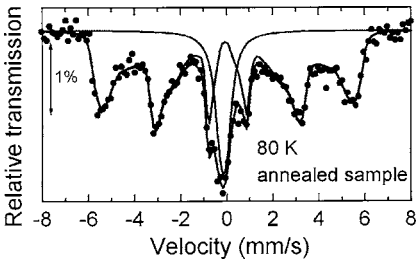

FIG. 9. Mössbauer spectrum recorded at 80 K of sample FeCr47.7 annealed at 700 K.

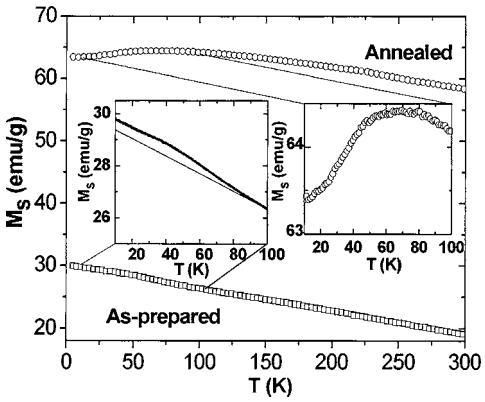

FIG. 10. Magnetization vs temperature for the as-prepared and annealed FeCr47.7 samples at a 1-T applied field. The insets show blow-ups of the curves.

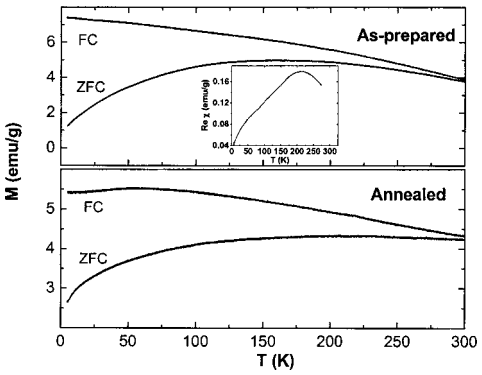

FIG. 11. ZFC-FC curves for the as-prepared and annealed FeCr47.7 samples at a 0.01-T applied field. The inset shows the temperature dependence of the real part of ac magnetic susceptibility.

However, T_C is not well defined, probably due to the existence of σ-FeCr nanoparticles of slightly different compositions, implying a distribution of T_C's, as well as the proximity effect due to neighboring with strongly magnetic α phase. In the case of the annealed sample, the contribution of the 30 wt % σ-FeCr phase is not observed but the inset reveals a local maximum at $T \sim 75$ K which may arise from the freezing in a spin-glass-like state of randomly oriented α-FeCr particles interacting with and across the antiferromagnetic Cr_2O_3 interface. Shown in Fig. 11 are the zero-field-cooled (ZFC) and field-cooled (FC) magnetizations versus T curves for the as-prepared and annealed samples measured at 100 Oe applied field. For the as-prepared sample, the ZFC curve exhibits a broad maximum at $T_B^{\mathrm{ZFC}} \sim 160$ K and does not overlap with the FC branch, which shows a progressive decrease of the magnetization with increasing temperatures. This indicates that while the smallest size α-FeCr particles are in the superparamagnetic state, the others form agglomerates and remain coupled by the long-range dipolar interactions thus being less susceptible to thermal fluctuations, in agreement with the results obtained by Mössbauer spectroscopy. The superparamagnetism is also evidenced by the ac susceptibility measurement performed in a 10 Oe ac field at a frequency of 1 kHz (see the inset) which presents a maximum at $T_B^{\mathrm{ac}} \sim 200$ K. The maxima of the ZFC magnetization and ac susceptibility curves indicate the average blocking temperature of the relaxing component. As expected, $T_B^{\mathrm{ZFC}} < T_B^{\mathrm{ac}}$ due to the larger measuring time of the magnetization measurements as compared to the ac susceptibility. In contrast, in the ZFC-FC curves of the annealed sample the temperature-activated processes are not seen and they present a behavior typical of a system of interacting particles.

As can be seen in Fig. 12, the annealed sample presents a higher coercivity (H_c) and thermoremanence (TRM) as a consequence of reordering of the system. Both samples present a rapid initial decrease of H_c and TRM as T is increased which can be ascribed to the transition of the σ phase to the paramagnetic state. Note that for as-prepared sample the decrease of H_c and TRM is more pronounced and takes place in a wider temperature interval than in the case of the annealed sample. This is in agreement with the fact that upon annealing the fraction of σ-FeCr has been reduced from 60 to 30 wt %. Above 100–150 K H_c is almost constant,

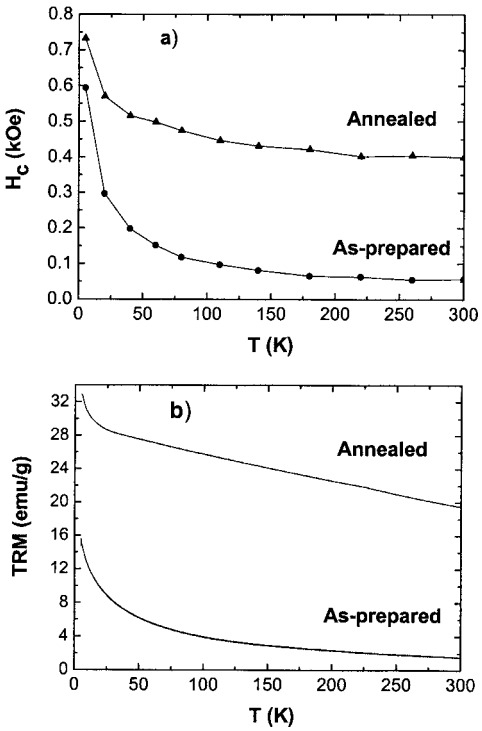

FIG. 12. (a) Coercive field and (b) thermoremanence vs temperature for the as-prepared and annealed FeCr47.7 samples.

evidencing that the bcc phase is not affected by thermal fluctuations. These results point out the role played by weak magnetic σ-FeCr in the coupling of α-FeCr ferromagnetic particles through the long-range dipolar interactions. For both samples, the hysteresis loops at 5 K obtained after cooling in 0 and 1 T applied fields overlap, indicating that there is no exchange bias due to the coupling between the antiferromagnetic Cr_2O_3 and the ferromagnetic bcc-FeCr. Exchange bias has previously been reported for 7 nm pure Fe nanoparticles embedded in a Cr_2O_3 matrix.[32] In our case, the absence of coupling can be explained on the basis of the low anisotropy constant of Cr_2O_3 and the small thickness (<5 nm) of this oxide shell.[33]

IV. CONCLUSIONS

It has been shown that α-FeCr and σ-FeCr high-temperature phases can be stabilized in a system of $Fe_{1-x}Cr_x$ nanoparticles prepared by thermal evaporation. The former is the major phase in all the studied compositions except for the 47.7 and 60.4 at. % Cr samples in which the σ-FeCr dominates. σ-FeCr phase is weakly magnetic with an average magnetic moment of $0.1\mu_B$ per Fe atom and the Curie temperature below ~60 K. The study of the Fe-Cr47.7 at. % sample has revealed that σ-FeCr is stable up to 550 K where it starts to transform to bcc-FeCr which, when annealed at 700 K, yields additionally Cr_2O_3 due to Cr segregation. In the as-prepared sample the separation of the α-FeCr particles and their agglomerates by the paramagnetic σ-FeCr phase results in the appearance of the superparamagnetic relaxation effects. In turn, the annealed sample, with largely reduced paramagnetic σ-FeCr phase, is less susceptible to the thermal fluctuations and its magnetic behavior is dominated by the

interparticle interactions. These interactions can be both of the exchange and dipolar origins and they extend across the antiferromagnetic Cr_2O_3 interface as well as the paramagnetic σ phase. The anisotropic character of the dipolar interactions as well as the spin-canting effects which can be expected at the ferromagnetic (α-FeCr)–antiferromagnetic (Cr_2O_3) interface results in the magnetic hardening of the annealed powder and the spin-glass-like freezing effects at low temperatures. Despite of the presence and proximity of the ferro- and antiferromagnetic phases in the annealed sample, the exchange bias has not been observed.

ACKNOWLEDGMENTS

This research has been supported by a NATO fellowship (OTSF03-074) and the CSIC-PAS exchange program (2004PL0009). C. Rovira (ICMAB-CSIC), for facilitating DSC measurements and E. Snoeck (CEMES-CNRS), for performing the HRTEM measurements, are acknowledged.

[1]A. Inoue and A. Takeuchi, Mater. Sci. Eng., A **375–377**, 16 (2004); K. Hashimoto, *ibid.* **226–228**, 891 (1997); W. Miller, M. J. Kramer, L. H. Lewis, L. M. Fabietti, Y. Tang, K. W. Dennis, and R. W. McCallum, J. Magn. Magn. Mater. **241**, 144 (2002).
[2]H. Pokhmurska, V. Dovhunyk, M. Student, E. Bielanska, and E. Beltowska, Surf. Coat. Technol. **151–152**, 490 (2002).
[3]M. Jones, A. J. Horlock, P. H. Shipway, D. G. McCartney, and J. V. Wood, Wear **249**, 246 (2001).
[4]W. Ruettinger, O. Ilinich, and R. J. Farrauto, J. Power Sources **118**, 61 (2003).
[5]H. Kurokawa, K. Kawamura, and T. Maruyama, Solid State Ionics **168**, 13 (2004).
[6]R. Sbiaa and H. Morita, Appl. Phys. Lett. **84**, 5139 (2004).
[7]*Binary Alloy Phase Diagrams*, edited by T. B. Massalski (American Society of Metals, Metals Park, OH, 1990), Vol. 1.
[8]A. A. Levin, D. C. Meyer, A. Teslev, A. Gorbunov, W. Prompe, and P. Paufler, J. Alloys Compd. **334**, 159 (2002).
[9]Yu. I. Petrov and E. A. Shafranovsky, Bull. Russ. Acad. Sci. Phys. **64**, 1236 (2000).
[10]L. Lutterrotti and S. Gialanella, Acta Mater. **46**, 101 (1997).
[11]H. L. Yakel, Acta Crystallogr., Sect. B: Struct. Sci. **39**, 20 (1983).
[12]R. A. Brand, Nucl. Instrum. Methods Phys. Res. B **28**, 398 (1987).
[13]K. Sumiyama, N. Ohshima, and N. Nakamura, Trans. Jpn. Inst. Met. **28**, 699 (1987).
[14]J. B. Kortright, S.-K. Kim, and H. Ohldag, Phys. Rev. B **61**, 64 (2000).
[15]N. H. Duc, A. Fnidiki, J. Teillet, J. Ben Yousef, and H. Le Gall, J. Appl. Phys. **88**, 4778 (2000).
[16]J. Cieślak, S. M. Dubiel, and B. Sepiol, Solid State Commun. **111**, 613 (1999).
[17]A. Blachowski, S. M. Dubiel, J. Zukrowski, J. Cieślak, and B. Sepiol, J. Alloys Compd. **313**, 182 (2000).
[18]S. M. Dubiel and B. F. O. Costa, Phys. Rev. B **47**, 12257 (1993).
[19]B. F. O. Costa, M. M. Pereira de Azevedo, M. M. Amado, J. B. Sousa, and N. Ayres de Campos, J. Alloys Compd. **297**, 15 (2000).
[20]S. M. Dubiel and J. Zukrowski, J. Magn. Magn. Mater. **23**, 214 (1981).
[21]F. B. Waanders and S. W. Vorster, Hyperfine Interact. **112**, 139 (1998).
[22]A. A. Levin, D. C. Meyer, A. Gorbunov, A. Mensch, W. Pompe, and P. Paufler, J. Alloys Compd. **360**, 107 (2003).
[23]Yu. I. Petrov and E. A. Shafranovsky, J. Nanopart. Res. **3**, 419 (2001).
[24]Yu. I. Petrov, E. A. Shafranovsky, Yu. F. Krupyanskii, and S. V. Essine, J. Appl. Phys. **91**, 352 (2002).
[25]E. Clauberg, J. Janovec, C. Uebing, H. Viefhaus, and H. J. Grabke, Appl. Surf. Sci. **161**, 35 (2000).
[26]J. Janssen, H. Rumpf, H. Modrow, R. Rablbauer, G. Frommeyer, and J. Hormes, Z. Anorg. Allg. Chem. **629**, 1701 (2004).
[27]B. F. O. Costa, G. Le Caër, and N. Ayres de Campos, Phys. Status Solidi A **183**, 235 (2001).
[28]A. Slawska-Waniewska, A. Roig, M. Gich, Ll. Casas, K. Racka, N. Nedelko, and E. Molins, Phys. Rev. B **70**, 054412 (2004).
[29]R. S. Preston, S. S. Hanna, and J. Heberle, Phys. Rev. **128**, 2207 (1962).
[30]D. A. Read, E. H. Thomas, and J. B. Forsythe, J. Phys. Chem. Solids **29**, 1569 (1968).
[31]J. Cieślak, M. Reissner, W. Steiner, and S. M. Dubiel, J. Magn. Magn. Mater. **272–276**, 534 (2004).
[32]J. Sort, V. Langlais, S. Doppiu, B. Dieny, S. Suriñach, J. S. Muñoz, M. D. Baró, Ch. Laurent, and J. Nogués, Nanotechnology **15**, S211 (2004).
[33]R. K. Zheng, H. Liu, Y. Wang, and X. X. Zhang, Appl. Phys. Lett. **84**, 702 (2004).